ADVANCED FUNCTIONAL MATERIALS
www.afm-journal.de

Materials Views
www.MaterialsViews.com

A Multi-synergistic Platform for Sequential Irradiation-Activated High-Performance Apoptotic Cancer Therapy

Zhaowei Chen, Zhenhua Li, Jiasi Wang, Enguo Ju, Li Zhou, Jinsong Ren, and Xiaogang Qu**

Artificial hyperthermia is an emerging technique to induce apoptotic cancer cell death. However, achieving effective hyperthermic apoptosis is often difficult, as cells typically acquire resistance to thermal stress. With the aid of sequential irradiation, highly integrated nanoassemblies based on reduced graphene oxide–ZnO nanoparticles–hyaluronic acid (rGo-ZnO-HA) can serve as a multi-synergistic platform for targeted high-performance apoptotic cancer therapy. The surface engineering of ZnO/graphene hybrid with multifunctional HA biomacromolecules simultaneously confers the system colloidal stability, biocompatibility, and a cancer cell targeting ability. After receptor-mediated endocytosis, enzyme-mediated fluorescence activation helps track cellular uptake and provides truly molecular imaging. Furthermore, the reactive oxygen species (ROS) generated by ZnO/rGo under light illumination can effectively sensitize cancer cells to the subsequent NIR laser-induced apoptotic hyperthermia. In particular, photo modulation of cellular ROS to sensitize cells provides a novel approach to increase the efficacy of hyperthermic apoptosis. These findings suggest that a powerful apoptotic therapeutic platform could be achieved based on the multi-synergistic platform.

1. Introduction

Apoptosis, unlike necrosis, is a more benign form of controlled cell death without releasing of harmful cellular waste, which minimizes inflammation and damage to surrounding cells.[1] Recent knowledge on apoptosis has made it possible to devise novel approaches that exploit this process for cancer therapy.[2] Generally, apoptosis occurs in tumour cells in response to therapeutics such as cytotoxic drugs, radiation, and hyperthermia.[2b,3] Ideally, the purpose of any cancer therapy is to eliminate cancer cells without harming healthy tissues. As for local thermal therapy, localized heating seems optimum at around 43 °C, where most normal tissues remain undamaged while cancer cells suffer apoptosis.[3,4] Unfortunately, the ability of cells to acquire transient resistance to thermal stress following a prolonged or fractionated ~43°C exposure would restrict the therapy efficiency.[5] Recently, to overcome the disadvantages, modulation of cellular ROS by various drugs called “thermosensitizers” has been demonstrated as a potential strategy to effectively sensitize cancer cells and make them more susceptible to apoptotic hyperthermia.[6] However, the lack of specificity of thermosensitizer drugs for tumor cells and the resulting toxicity to normal tissue would hamper further exploitation of their apoptotic effects.

Nowadays, advances in nano-biotechnology have allowed the combinations of various functional components to offer multimodality theranostic platforms.[7] Of particular interest with this class of materials is the ability to integrate discrete therapeutics into one platform and achieve higher oncolytic efficacy than that of each single mode. Among all the anticancer treatments, photodynamic therapy (PDT) and photothermal therapy (PTT) involving light induced cytotoxicity have unique advantages, including remarkable spatial/temporal resolutions, improved selectivity and reduced side effects.[8] For PDT, photosensitizers (PSs) can produce ROS that cause an effective and selective destruction of diseased tissues. For PTT, its implementation relies on the development of photothermal agents generating heat from light absorption. Hence, there is great potential to establish PDT/PTT integrated platforms for enhanced cancer therapy while sparing normal tissues. Although researchers have made great efforts to combine PS with near-infared (NIR) absorbing agents such as graphene and gold nanostructures for PDT/PTT,[9] limitations still exist: 1) most nanoassemblies require complicated synthetic process, which means expensive human and material costs; 2) extra steps are needed to loading PS, where the loading efficiency is always variable and highly dependent on the loading conditions and the inherent structure of the vectors; 3) energy transfer between PS with hyperthermia agents can quench the PS and inhibit the production of ROS, restricting the anticancer efficiency; 4) high temperature (>45°C) is often involved in PTT, which would induce necrosis and unnecessary

---

Z. Chen, Z. Li, J. Wang, E. Ju, L. Zhou,
Prof. J. Ren, Prof. X. Qu
State Key laboratory of Rare Earth Resources Utilization
and Laboratory of Chemical Biology
Changchun Institute of Applied Chemistry
Chinese Academy of Sciences
Changchun 130022, China
E-mail: jren@ciac.jl.cn; xqu@ciac.jl.cn

Z. Chen, Z. Li, J. Wang, E. Ju, L. Zhou, Prof. J. Ren, Prof. X. Qu
Graduate School of the Chinese Academy of Sciences
Beijing, 100039, China

DOI: 10.1002/adfm.201301951

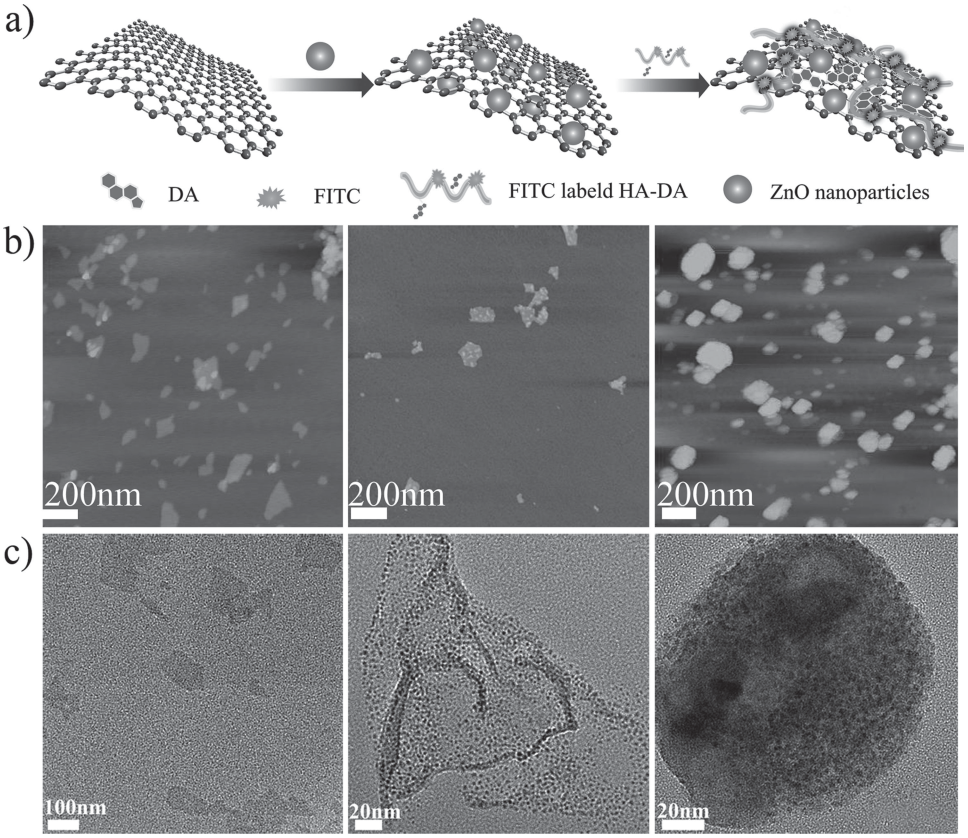

Figure 1. a) Schematic representation of synthesis of rGo-ZnO-HA (or FITC labeled HA) assemblies. b) and c) are AFM and TEM micrographs of Go, rGo-ZnO and rGo-ZnO-HA (from left to right), respectively.

heating of normal tissues; 5) lack of specificity would result in unavoidable damage to nontarget cells. Taken together, it is of great importance to search for a novel class of nanoassemblies to overcome the aforementioned drawbacks and re-explore a new mechanism to obtain synergistic cancer therapy.

Toward this goal, herein, for the first time, we develop a new design of highly integrated nanoplatform based on rGo-ZnO-HA assemblies (**Figure 1**a) for targeted high-performance apoptotic cancer therapy. The primary motivations for employing ZnO nanoparticles lie in the fact that they are easy to fabricate, inexpensive, also they themselves exhibit active therapeutic effect.[10] Especially, due to its unique phototoxic effect, ZnO has been regarded as attractive ROS sensitizing agents for anticancer or antibacterial studies, which is mainly based on its ability to produce electron-hole pairs upon light illumination and thereby create highly reactive oxygen species.[11] Of particular interest, the photo activities of ZnO nanoparticles could be significantly enhanced by hybrid with graphene, where graphene acts as excellent electron acceptors to inhibit the quick recombination of the photoexcited electron-hole pairs and so enhance the generation of ROS.[12] In addition to its electrical properties, graphene has been used as a versatile photothermal agent owing to its high optical absorption in the NIR region.[9a,13] Inspired by these unique features, herein, we propose a conceptually new approach: by utilizing sequential irradiation as stimuli, the ROS generating by rGo-ZnO under light illumination can effectively sensitize cancer cells to the subsequent NIR laser induced hyperthermia for realizing high-performance apoptosis. Yet, proper surface engineering (e.g., biocompatible coatings) of graphene-based nanocomposites (GNC) is vital for potential biomedical applications.[13b] As one of the extracellular matrix components, HA possesses several advantages: it is biodegradable, non-toxic, and can be easily chemically modified with imaging or other functional groups.[14] Intriguingly, HA has been used as a drug carrier or targeting moiety due to the specific interaction with CD44, which is overexpressed on various cancer cells.[15] Such uniqueness, when conjugated on GNC, not only affords GNC colloidal stability but also biocompatibility and cancer target ability. Moreover, HA could be specially degraded by intracellular enzyme hyaluronidase-1 (Hyal-1) after receptor mediated endocytosis,[14a,b,15d,16] which could be utilized to track GNC cellular uptake or for bio-imaging through the release of fluorophore-labelled HA fragments from graphene surface. Thus, the integration of these functionalities makes this nanoassembly a potentially new tool for targeted cancer imaging and treatment through sequential irradiation activated apoptotic therapy.

2. Results and Discussion

In this work, graphene oxide (Go) was obtained according to a modified Hummer's method.[17] As depicted in supporting information, rGo-ZnO nanohybrids were obtained by assembling ZnO nanoparticles (Figure S1) on graphene nanosheets at water/toluene interface. Atomic force microscopy (AFM, Figure 1b) and transmission electron microscopy (TEM) images (Figure 1c) clearly shows that ZnO nanoparticles were evenly distributed on the surface of graphene sheet. In addition, compared with Go, the appearance of Zn2p peaks as well as the reduction of oxygen-containing groups in X-ray photoelectron spectroscopy (XPS) data (Figure S2) further indicated the successful synthesis of rGo-ZnO nanocomposites. Also, compared with as-prepared Go, rGo-ZnO nanocomposites exhibited increased light absorption in the visible and NIR region (Figure S3) which was favourable for applications in PTT. In order to increase the colloidal stability of the nanocomposites, amphiphilic hyaluronic acid-deoxycholic acid (HA-DA) was synthesized (Figure S4) and used to surface engineer the nanohybrids through the hydrophobic interactions between DA and graphene, forming rGo-ZnO-HA with excellent biocompability and cancer cell targeting ability. The lateral size of the final nanocomposites ranged from 100–250 nm (with a mean of ~226 nm) determined by AFM, TEM and dynamic light scattering experiment (Figure 1 and Table S1). The successful conjugation of HA was evidenced by Fourier-transform infrared spectroscopy (FTIR; Figure S5) and XPS (Figure S2). According to the thermo gravimetric analysis (Figure S6), the mass ratio of rGo: ZnO: HA-DA was 1: 1.1: 0.9. Zeta-potential measurements (Table S1) of the nanoassemblies showed a negative charge of –69.4 ± 3.8 mV, further implying the conjugation of HA on the surface of the nanohybrids. Typically, zeta potentials below –30 mV are considered as an indication of a colloidal stable system.[18] The strongly negative-charged surface confers the nanoconjugates excellent stability in buffers and other biological solutions over a long period without any precipitation (Figure S7). This favourably provides additional advantages for blood circulation and the tumor accumulation of nanoparticles by the enhanced permeation and retention (EPR) effect of well-dispersed nanoconjugates.

For cancer cell targeted imaging, FITC labelled HA-DA (HA-F) was synthesized (Figure S8) and assembled with rGo-ZnO (Figure 1a, Figure S9). Due to the high optical absorbance of graphene, close proximity of HA-F to graphene sheets in the nanoassemblies was expected to result in strong fluorescence quenching. However, HA is readily degraded into low molecular weight fragments by Hyal-1 whose levels are known to increase in tumor microenvironment.[15d] We expected that this enzyme mediated degradation would reactivate the fluorescence of HA-F. To test the hypothesis, fluorescence titration experiment was first carried out to evaluate the interaction between HA-F and rGo-ZnO. As shown in Figure S10, the fluorescence signals decreased promptly as the rGo-ZnO concentration was increased. Next, we explored the effects of Hayls on the fluorescence recovery of rGo-ZnO-HA-F nanocomposites. The presence of Hyals gave a strong fluorescence which was dependent on both time and enzyme concentration (**Figure 2**). To further confirm that enzymes were responsible for the recovery, two additional experiments were carried out (Figure S11). In one experiment, the enzyme was denatured by heating enzyme solutions at 90 °C for 60 min before addition to the nanoassemblies. As expected, no fluorescence recovery was observed. In another experiments, we found that the rGo-ZnO-HA-F composite showed only slight fluorescence enhancement upon incubation with bovine serum albumin (BSA) contained cell culture medium. We ascribed this effect to the strong affinity of HA-F to graphene as a result of multivalent interactions between the multiple DA moieties on HA backbone and graphene surface. These findings, therefore, validated that enzymatic degradation of HA was responsible for the recovery of fluorescence other than displacement of HA caused by nonspecific protein adsorption, which predicted its potential use for tracking the nanocomposite cellular uptake or for bioimaging.

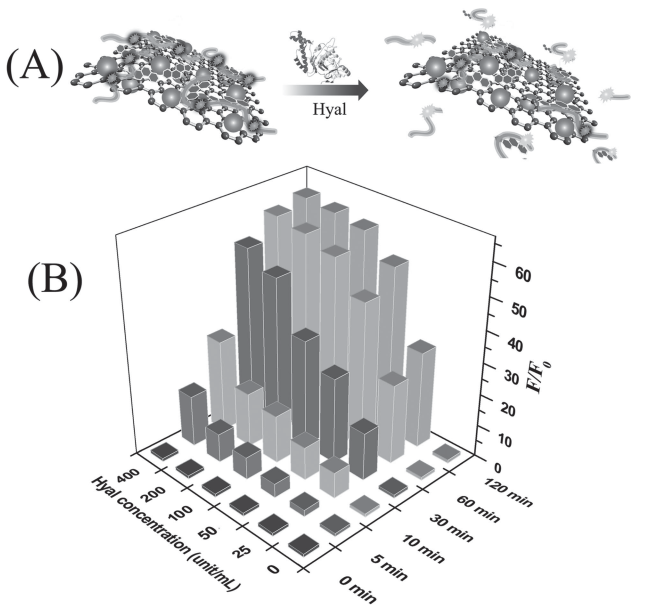

Figure 2. a) Schematic illustration of enzyme activated fluorescence recovery. b) Fluorescence intensity fold changes of rGo-ZnO-HA-F over different concentrations of enzyme and time. The results from representative of at least three experiments are presented.

Next, to confirm the target ability of the nanoassemblies, MDA-MB-231 cells (CD44 overexpressed) and NIH3T3 cells (normal cells) were chosen as target cancer cells and control cells, respectively. Cells were treated with rGo-ZnO-HA-F for 0.5h, 1.5h, and 3h. It is evident from flow cytometry experiments (**Figure 3**) that a time-dependent fluorescence enhancement was observed for MDA-MB-231 cells, implying the special interaction between HA and CD44 overexpressed on MDA-MB-231 cells and Hayl mediated fluorescence activation. As for NIH3T3 cells, neither enhancement nor time dependency was observed, which was mainly attributed to lack of CD44 receptors and a lower level of intracellular Hyal-1.[14a] Corresponding confocal fluorescence microscopy images were consistent with the FACS results: a strong green fluorescence was observed for MDA-MB-231 cells, but no distinct fluorescence was seen for NIH3T3 cells (Figure 3f). Moreover, competition experiments, using 5 mg/mL free HA, were performed as described previously.[15a] As shown in Figure 3e, no significant fluorescence was observed, which indicates that CD44 receptors are responsible for the efficient cellular uptake of rGo-ZnO-HA-F. Thus, the conjugation of HA successfully renders the system cancer cell target ability. In other words, the design renders the system the ability for target cancer therapy.

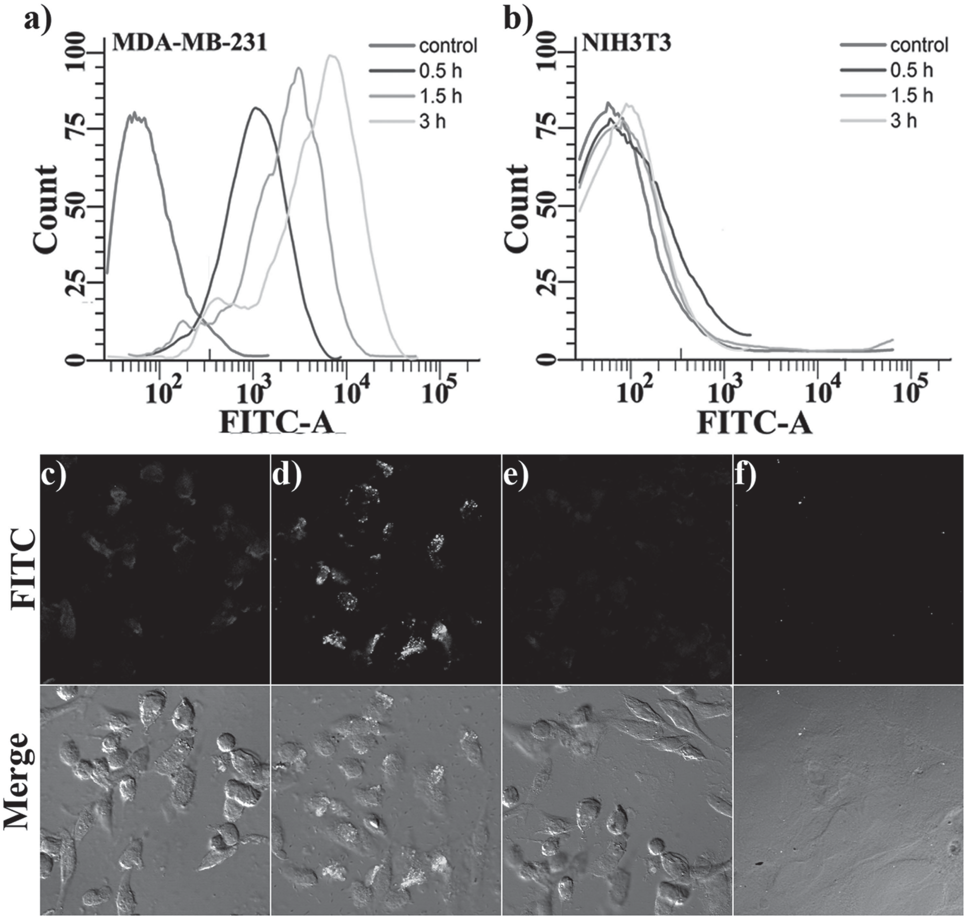

Figure 3. a) and b) Fluorescence-activated cell sorting (FACS) distribution of fluorescence in each cell type after 0.5 h, 1.5 h and 3 h treatment with rGo-ZnO-HA-F. Confocal fluorescence imaging of cells incubated with rGo-ZnO-HA-F: c) and d) MDA-MB-231 cells for 0.5 h and 3 h, respectively, e) MDA-MB-231 cells for 3 h after preincubation for 2 h with free HA (5 mg/mL), f) NIH3T3 cells for 3 h.

Having demonstrated the internalization experiments, we were in a position to evaluate the toxicity of the rGo-ZnO-HA. The standard methyl thiazolyl tetrazolium (MTT) assay was carried out to evaluate the cytotoxicity of rGo-ZnO-HA in incubated MDA-MB-231 and NIH3T3 cells with various concentrations for 24 h. The results (Figure S12) revealed negligible toxicity towards NIH3T3 cells even at high concentrations up to 200 μg/mL, whereas rGo-ZnO-HA exhibited certain cytotoxic effect against MDA-MB-231 cells, most notably at 200 μg/mL. As an indicator of oxidative stress in cells, the ROS levels were measured by staining cells with 2,7-dichlorofluorescein diacetate (DCFH). The flow data (Figure S12a) showed that cancer cells expressed an elevated ROS with increasing rGo-ZnO-HA, while NIH3T3 cells remained unaffected. Several reports on nanotoxicology have suggested the elevated level of ROS caused by graphene[19] or by ZnO[10b,c] lead to cell death. Especially, ZnO alone has been utilized as an anticancer therapeutic agent due to the Zn^{2+} ions induced oxidative stress.[10b] In further control experiments (Figure S12c), rGo-ZnO exhibited no significant cytotoxic difference towards both cancer and normal cell lines. However, compared with rGo-ZnO-HA, rGo-ZnO exhibited higher toxicity toward NIH3T3 cells and lower toxicity toward MDA-MB-231 cells at corresponding concentrations, which indicated the necessity of HA for target cancer cells while sparing normal tissues. Although, much emphasis has been put on adverse effect of nanomaterials, the direct utilization of nanomaterials as "active therapeutic agent" is rarely reported. Instead, herein, surface engineering of HA would help to "activate" the nanoassemblies toward cancer cells while minimizing side effects on normal cells, which added profound advantages for potential biomedical applications.

Motivated by the fact that semiconductive nanomaterials are potent enough to sensitize the production of ROS and their good combination with graphene improves photo activities, we anticipated that a novel killing mode, that is, PDT mediated cell killing would be realized. DCFH was utilized in our experiment to prove the generation of ROS from the photocatalyst under light irradiation. As shown in Figure S13, rGo-ZnO exhibited a remarkable enhancement in the ROS generation compared with ZnO nanosphere under light irradiation, which agrees well with previous reports.[12b,c] For the sake of minimizing side effects, 0.5 h light irradiation was employed for the cellular photosensitization experiments (Figure S14). After incubation MDA-MB-231 cells with

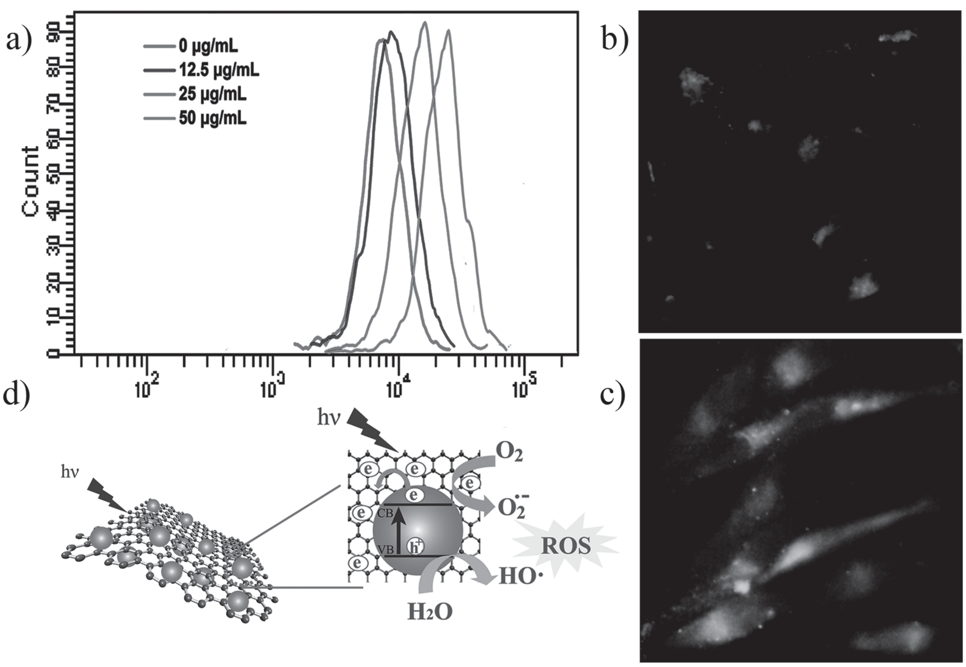

Figure 4. a) Flow cytometry analysis of light induced ROS generation after MDA-MB-231 cells treated with various concentrations of rGo-ZnO-HA. b) and c) are microscopy images of light induced ROS generation of MDA-MB-231 cells treated with 0 and 25 µg/mL rGo-ZnO-HA, respectively. d) Mechanical illustration of ROS generation for rGo-ZnO hybrids under light irradiation.

rGo-ZnO-HA for 4 h, light induced intracellular ROS accumulation detected by flow cytometry increased in dose dependent manner (**Figure 4**a). Microscopy study also showed bright green fluorescence resulting from the oxidized form of DCFH within the intracellular regions of cancer cells (Figure 4b,c); further confirming the sensitization of ROS by rGo-ZnO in cancer cells. The schematic illustration of ROS generation mechanism by rGo-ZnO is summarized in Figure 4d. Under the light illumination, ZnO was excited to form electron-hole pairs, which separated at the interfaces of ZnO and rGo sheets. The electrons can transport along the superior-conduct rGo nanosheets, which decrease the rate of recombination of the photo excited pairs and so increase the quantum efficiency of the photosensitization process. These electrons and holes would induce a series of reactions generating ROS. Herein, due to its low tissue penetration ability, 365 nm irradiation to activate rGo-ZnO hybrid is only used as a proof of concept. For broadened applications, various methods[20] such as ion doping can be expected to extend the light absorption range ZnO-rGo hybrids for enhanced visible-light-driven activities, which is however beyond the scope of this study.

On the other hand, due to its strong NIR adsorption, the rGo-ZnO could be sufficient to afford efficient hyperthermia therapies. When exposed to 808nm NIR laser, the solution of rGo-ZnO exhibited a concentration- and radiant energy-dependent photothermal heating effect (Figure S15). Thus, encouraged by the uniqueness of the nanoassembly, we anticipated that a synergistic apoptotic therapy would be achieved by a sequential irradiation process: ROS generated during the PDT can effectively sensitize cancer cells and improve the subsequent mild photothermal treatment (**Figure 5**a). To verify the hypothesis, cell viability assay, represented in Figure 5b, shows the percentage of cell survival after treatment of rGo-ZnO-HA incubated cancer cells with light irradiation followed by photothermal heating at 43 ± 1 °C for 30 min. Note that PDT or PTT alone only induced a moderate growth inhibition of MDA-MB-231 cells. In contrast, the combination of PDT and PTT resulted in a significant cytotoxicity that was increased in a dose-dependent manner. Also, the efficacy of the combined PDT/PTT treatments is significantly higher than the additive therapeutic efficacy of PDT and PTT treatments, which were estimated using the relation of $P_{additive} = (f_{PDT} \times f_{PTT}) \times P_0$, where $P_{additive}$ is the final population after an additive interaction, P_0 is the initial population and f is the fraction of surviving cells after each treatment. To further demonstrate that the ROS generated by PDT increases PTT-induced cytotoxicity, cells were exposed to increase dose of H_2O_2 prior to PTT conditions. Similar to the combination of PDT and PTT, there was a significant increase in cell death (Figure S16) compared with H_2O_2 or PTT alone. Also, to compare with NIR photothermal heating, cells were heated thermally in a water bath to ~43 °C for 30 min (Figure S16c). Cell viability proved to be similar to the laser irradiated case. Moreover, rGo-ZnO-HA showed significantly higher efficacy in tumour reduction compared to rGo-ZnO (Figure S16a), mainly because the HA targeting property allowed a higher amount of rGo-ZnO-HA to bind to the cell surface and to be internalized by the MDA-MB-231 cells, whereas the non-targeted rGo-ZnO was only endocytosed to a very limited extent. The results indicated the ability of our assemblies for targeted cancer therapy.

We next explored the possible death mechanism by flow cytometry experiments using annexin V-fluorescein isothiocyanate (Annexin V-FITC) and propidium iodide (PI) staining assay

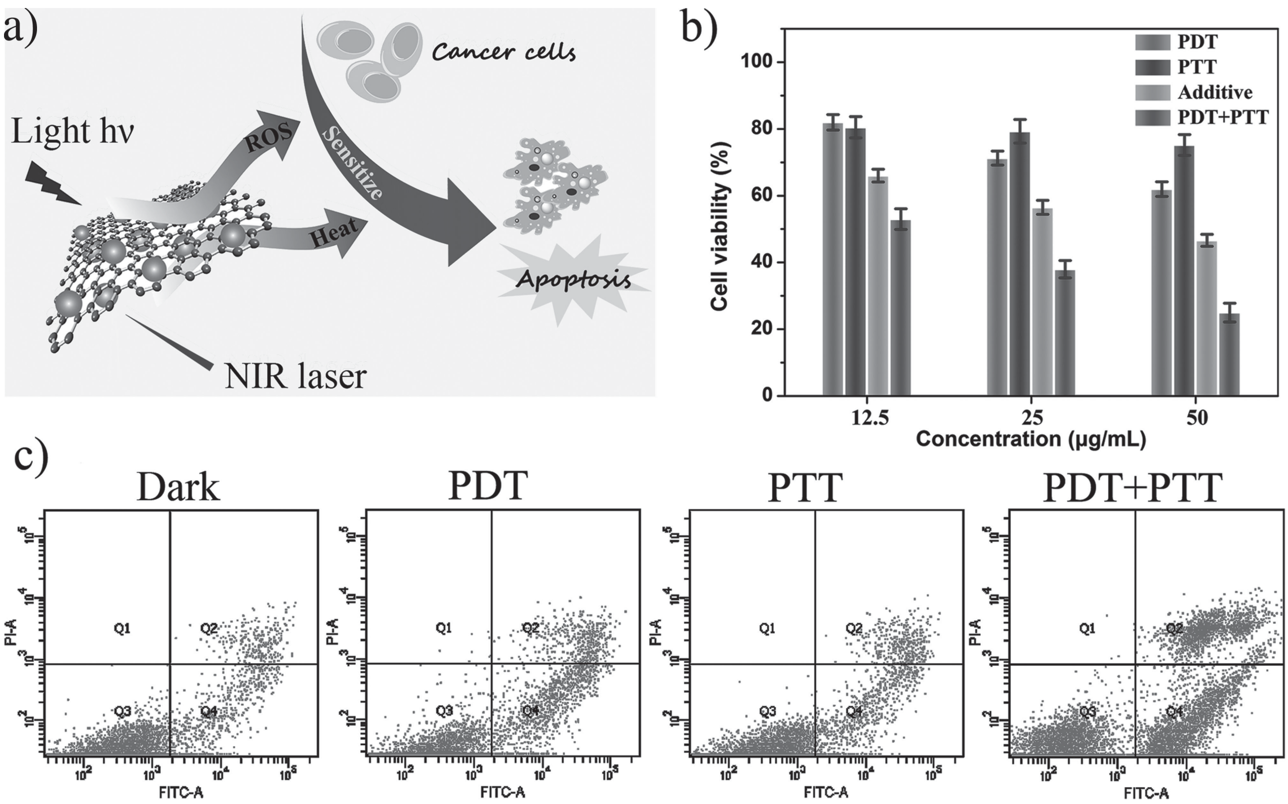

Figure 5. a) Schematic illustration of the sequential irradiation activated high-performance apoptosis. b) In vitro cell ability of MDA-MB-231 cells treated with rGo-ZnO-HA following PDT, PTT and combined PDT/PTT treatments. The efficacy of combined treatment is compared with the additive efficacy of independent PDT and PTT treatments using t-tests with all p-values lower than 0.05. c) Flow cytogram representing apoptosis assay based on Annexin V-FITC and PI staining of cells treated with 25 μg/mL rGo-ZnO-HA followed by photo treatment. In the flow cytogram, the cells in Q3 region denotes live cells, Q4: apoptotic, Q2: late apoptotic and Q1: necrotic cells.

(Figure 5c). Annexin V-FITC can identify apoptotic cells by binding to phosphatidylserine translocated from the inner to the outer leaflet of the cell membrane, whereas PI is impermeant to live cells and early apoptotic cells. Apoptosis in dark conditions could be attributed to the endocytosed nanomaterial's toxicity.[19,10b] Corresponding with the MTT results, significantly higher proportion of cell population treated with combination of PDT and PTT is Annexin V-FITC positive as compared to that of the two therapies independently. These results evidently substantiated that PDT mediated ROS efficiently sensitized cancer cells and enhanced the subsequent mild photothermal induced apoptosis. Accordingly, compared to the previous heat sensitizers, modulation of cellular ROS by PDT provide a novel approach for improving thermal apoptosis efficiency. More importantly, the light stimulated therapeutics possesses unique advantages including high selectivity, spatial/temporal controllability; in this way, off-target effects were minimized. Taken together, we confirmed our hypothesis that the rGo-ZnO-HA nanoassemblies could serve as a novel multi-synergistic platform for enhanced apoptotic cancer therapy based on programmable photo activated process.

3. Conclusions

We have demonstrated the first example that the highly integrated rGo-ZnO-HA nanocomposite could serve as a multi-synergistic platform for targeted high-performance apoptotic cancer therapy by utilizing sequential irradiation as stimuli. The photocatalytically active ZnO/graphene hybrid created highly reactive oxygen species under light irradiation, which effectively sensitized cancer cells to the following apoptotic hyperthermia by rGo under NIR laser irradiation. Compared with traditional drug strategies, photo modulation of cellular ROS to sensitize cells represents a novel approach to increase the efficacy of hyperthermic apoptosis. Moreover, the tri-component nanoassemblies not only display cooperative properties but also maintaining the individual properties of each constituent, which overcomes several of the obstacles mentioned above. First, the graphene hybrid itself not only acts as a PDT agent but also as PTT agent, which means simple designing. Second, unlike conventional PS, the combination of ZnO and rGo effectively improves the ROS generation instead of quenching. Third, the adherence of HA onto rGo-ZnO hybrids not only affords the system colloidal stability but also biocompatibility and cancer cell target ability. This synergistic effect provides a new way to fine-tune the biochemical properties of graphene based nanocomposites by simply using different functional groups tagged HA. Finally, the ability of intracellular enzyme activated fluorescence is an extra surprise to enrich the function of this system, which can help tracking cellular uptake and provide truly molecular imaging. Combined together, a powerful theranostic platform could be achieved based on the multi-synergistic platform.

4. Experimental Section

Materials: Nanopure water (18.2 MΩ; Millpore Co., USA) was used in all experiments and to prepare all buffers. 1-Ethyl-3(3-dimethylaminopropyl) carbodiimide (EDC), deoxycholic acid, *N*-hydroxysuccinimide (NHS) were purchased from Sigma Aldrich (Saint Louis, Missouri, United States). Fluorescein isothiocyanate (FITC) was obtained from Alfa Aesar. Sodium hyaluronate (MW≈200KDa) and adipic dihydrazide were purchased from Aladdin. Trypsin, Dulbecco's modified Eagle's medium (DMEM), fetal bovine serum (FBS), and hyaluronidase (Hyal) from bovine vitreous humor were purchased from Shanghai Sangon Biological Engineering Technology & Services (Shanghai, China). All chemical agents were of analytical grade.

General Techniques: FT-IR analysis was carried out on a Bruker Vertex 70 FT-IR Spectrometer. TEM images were acquired with a TECNAI G2 transmission electron microscope (Philips Electronic Instruments Co. the Netherlands) at 200 kV. AFM measurements were performed using Nanoscope V multimode atomic force microscope (Veeco Instruments, USA). UV–Vis spectroscopy was carried out with a JASCO V-550 UV–Vis spectrometer. Fluorescence measurements were carried out on a JASCO FP-6500 spectrofluorometer. A CW diode laser (LSR808NL-2000) with a wavelength of 808 nm was used for the laser irradiation experiment.

Synthesis of rGo-ZnO Nanohybrids: Go was synthesized from graphite by modified Hummers method. Go nanosheet suspension was collected after probe-sonication for 4 h and centrifugation at 10 000*g*. Oleate-capped zinc oxide (ZnO) nanoparticles were preapared as previously reported.[21a] Then, Go (30 mg) in deionized water (50 mL) were added into a 250 mL flask. The mixture was then sonicated for 15 min to yield a yellow-brown solution. ZnO nanoparticles (50 mg) were dispersed in toluene (50 mL) was then added into the flask. The mixture was kept vigorously stirring for 3 h at room temperature. Then, 20 µL hydrazine was added into the suspension and mainatained at 80 °C for 12 h. The suspension exhibited a distinct color change from yellow-brown to black after reaction. The as-prepared rGo–ZnO were purified with large amounts of acetone and centrifuged for 10 min at 10 000 rpm three times. The final rGo–ZnO hybrids were then freeze-dried at –50 °C for 48 h.

Synthesis of Hyaluronic Acid–Deoxycholic Acid (HA-DA) Conjugates: Amphiphilic HA-DA conjugates were prepared by chemical grafting deoxycholic acid (DA) to adipic dihydrazide modified HA (HA-ADH) through amide formation as previously reported.[21b] The degree of substitution which is defined as the number of deoxycholic acid molecules per 100 sugar residues of HA was estimated using ^{1}H NMR in D_2O/CD_3OD (1 v/1 v). The chemical structures of HA-DA conjugates were confirmed using 1H NMR, as shown in Figure S4. The characteristic peaks of HA appeared at 2.01 ppm and 3.28–4.75 ppm, whereas those of adipic dihydrazide were found at the range of 1.63–1.79 ppm, 2.19–2.45 ppm. Successful introduction of DA into HA polymers was confirmed by the peaks of DA, which appeared at 0.67–1.60 ppm. The amount of DA in the conjugate was quantitatively characterized from the integration ratio between the characteristic peak of the *N*-acetyl group in HA (δ = ~2 ppm [3H, -$COCH_3$-]) and that of the methyl group in DA (δ = ~0.68 ppm [3H, -CH_3]). The degree of substitution (defined as the number of DA per 100 sugar residues of HA polymer) value was around 12% for HA-DA conjugates. For cellular imaging, fluorescein isothiocyanate (FITC) labeled HA-DA (HA-F) was synthesized. At the end of HA-DA conjugation experiments, FITC (2 mg) in 2 mL of DMF was added to the mixture, and the reaction was stirred at room temperature overnight. HA-F was purified by dialysis against 50% acetone/H_2O. The amount of conjugated FITC onto HA backbone was determined using the UV-Vis spectrometer by measuring absorbance at 493 nm and about 23 FITC molecules were conjugated to each HA chain (Figure S5).

Synthesis of rGo-ZnO-HA Assemblies: To conjugate HA-DA onto rGo-ZnO hybrids, 4 mg of the obtained rGo-ZnO hybrids were dispersed by sonicating with 2 mg/mL HA-DA solution (5 mL) for 1 h. To avoid heating, the solution was immersed in an ice-bath during sonication. The resulting solution was filtered through a 0.1 µm pore-sized microporous membrane to remove free HA-DA and the obtained product was dispersed in PBS buffer and then stored at 4 °C until further use.

Enzyme Activated Fluorescence Recovery Experiments: Hayl-activated fluorescence recovery was monitored by spectrofluorometer (JASCO FP-6500). Fluorescent quantification data of rGo-ZnO-HA-F solutions were obtained after the rGo-ZnO-HA-F solutions were incubated with different concentrations (0–400 unit/mL) of Hyal in an acetate buffer (pH = 6.0, 37 °C) for different time. The excitation wavelength was 493 nm and the emission wavelengths were in the range from 500 to 650 nm.

Cell Culture: MDA-MB-231 and NIH3T3 cells were cultured in 25 cm^2 flasks in Isceve's Modified Dulbecco's medium (IMDM) (Gibco) containing 10% (v/v) fetal bovine serum (Gibco) at 37 °C in an atmosphere of 5% (v/v) CO_2 in air. The media was changed every three days, and the cells were passaged by trypsinization before confluence.

Confocal Laser Scanning Microscopy (CLSM): FITC exhibits intense green fluorescence under UV light. This property allows the use of fluorescence to study the cellular uptake of rGo-ZnO-HA. MDA-MB-231 and NIH3T3 cells, incubated with rGo-ZnO-HA-F in medium for 0.5 h, 1.5 h, and 3 h, were next washed three times with PBS and transferred to serum-free medium and examined by CLSM. To confirm the binding of assemblies to the HA-receptors over-expressed on tumour cells surface, free HA was added 2 h before the addition of rGo-ZnO-HA-F. The fluorescence micrographs shown are representative of at least three independent experiments.

Detection of Intracellular ROS: Intracellular ROS generation was measured using an oxidation sensitive dye 2,7-dichlorofluorescein diacetate (DCFH); DCFH is a non-fluorescent compound that undergoes intracellular deacetylation, followed by ROS mediated oxidation to a fluorescent dichlorofluorescin (DCF). The oxidation product of DCFH has excitation/emission maxima of 495 nm/529 nm enabling detection using flow cytometry and confocal laser scanning microscopy. After various experimental treatments, cells were incubated with DCFH for 30 min and intracellular ROS generation was evaluated using flow cytometry.

Cell Viability Assay: MTT assay was used to evaluate the mitochondrial activity according to the protocol developed by Mossman. When cells reached 80% confluency, they were harvested and were seeded in 96 well plates (10^4 cells per well) and incubated for 24 h. Optical absorbance was measured in a microplate spectrophotometer at 570 nm with 660 nm set as the reference wavelength. Cell viability was calculated by the following equation: $[A]_{test}$ / $[A]_{control}$×100, where $[A]_{test}$ was the absorbance of the test cells treated with therapeutics and $[A]_{control}$ was the absorbance of cells without treatment. The results were expressed as percentage viability compared to the untreated controls. To evaluate the cytotoxicity of rGo-ZnO-HA, the cells were incubated with various concentrations of rGo-ZnO-HA in dark conditions for 24 h and MTT assay was performed.

Sequential Irradiation-Induced Cytotoxicity and Cell Viability Examination: Cells were grown as indicated above in 96-well plates to reach 10^4 cells per well. Cells were then washed 3 times with PBS and incubated with rGo-ZnO-HA nanoassemblies for 4 h. After 4 h cells were washed several times with PBS to eliminate unbound nanomaterials. For photodynamic therapy (PDT), the plates were illuminated for 30 minutes by 365 nm light (5 mW/cm^2). For photothermal therapy (PTT), the cells were irridiated with 808 nm laser. During the laser irradiation period, temperatures were closely monitored using thermoprobe, and the laser power was adjusted to maintain the temperature of culture medium at 43 ± 1 °C for 30 min. For sequential irradiation treatment, after PDT, cells were immediately irradiated using the 808 nm for 30 min and the temperature maintained at 43 ± 1 °C. The power density was variable from 20 to 400 J/cm^2. After light treatment, cells were incubated in a humidified atmosphere with 5% CO_2 at 37 °C. After further 24 h incubation, the standard MTT assay was carried out to determine the cell viabilities relative to the control untreated cells.

Detection of Apoptosis: Annexin V–FITC and PI assay was employed to detect apoptotic and necrotic cells. The assay consists of FITC conjugated Annexin V antibody, which is a 35–36 kDa Ca^{2+} dependent phospholipid-binding protein that has a high affinity for the membrane phospholipid phosphatidylserine (PPS) and binds to cells with exposed PPS. In normal viable cells the PPS is directed into the cytoplasm and upon initiation of programmed cell death, the PPS flips and get expressed on outer leaflet of the plasma membrane. In addition, cells are incubated with propidium iodide (PI), which differentiates apoptotic and necrotic cells. Using both dyes in combination with two-wavelength flow cytometry, they identify the apoptotic (Annexin V+) and necrotic cells (PI+) separately. At 24 h post photo treatment, cells were washed and stained with Annexin V and PI. Typically 1×10^5 cells were resuspended in 100 μL of binding buffer and 5 μL of FITC-conjugated Annexin V (Annexin V–FITC) and 5 μL of propidium iodide (PI) were added sequentially at room temperature in the dark. After incubation for 15 min, stained cells were diluted with 400 μL of binding buffer and directly analyzed by flow cytometry.

Acknowledgements

Financial support was provided by the National Basic Research Program of China (2011CB936004 and 2012CB720602) and the National Natural Science Foundation of China (21072182, 91213302, 21210002).

Received: June 7, 2013
Revised: June 28, 2013
Published online: October 22, 2013

---

[1] a) E. L. Taylor, I. L. Megson, C. Haslett, A. G. Rossi, *Cell. Death. Differ.* **2003**, *10*, 418; b) T. S. Hauck, T. L. Jennings, T. Yatsenko, J. C. Kumaradas, W. C. W. Chan, *Adv. Mater.* **2008**, *20*, 3832.

[2] a) C. G. Ferreira, M. Epping, F. A. E. Kruyt, G. Giaccone, *Clin. Cancer Res.* **2002**, *8*, 2024; b) K. M. Debatin, *Cancer Immunol. Immunother.* **2004**, *53*, 153.

[3] K. L. O'Neill, D. W. Fairbairn, M. J. Smith, B. S. Poe, *Apoptosis* **1998**, *3*, 369.

[4] a) J. van der Zee, *Ann. Oncol.* **2002**, *13*, 1173; b) B. V. Harmon, A. M. Corder, R. J. Collins, G. C. Gobé, J. Allen, D. J. Allan, J. F. R. Kerr, *Int. J. Radiat. Biol.* **1990**, *58*, 845.

[5] a) E. W. Gerner, M. J. Schneider, *Nature* **1975**, *256*, 500; b) J. T. Beckham, G. J. Wilmink, S. R. Opalenik, M. A. Mackanos, A. A. Abraham, K. Takahashi, C. H. Contag, T. Takahashi, E. D. Jansen, *Lasers Surg. Med.* **2010**, *42*, 912.

[6] a) C. C. Wang, F. Chen, E. Kim, L. E. Harrison, *Surgery* **2007**, *142*, 384; b) F. J. Li, T. Kondo, Q. L. Zhao, K. Tanabe, R. Ogawa, M. Li, Y. Arai, *Free Radical Res.* **2001**, *35*, 281; c) D. Y. Yu, Y. Matsuya, Q. L. Zhao, K. Ahmed, Z. L. Wei, T. Hori, H. Nemoto, T. Kondo, *Apoptosis* **2008**, *13*, 448; d) D. Yoo, H. Jeong, C. Preihs, J. S. Choi, T. H. Shin, J. L. Sessler, J. Cheon, *Angew. Chem.* **2012**, *124*, 12650; *Angew. Chem. Int. Ed.* **2012**, *51*, 12482.

[7] a) S. P. Sherlock, S. M. Tabakman, L. Xie, H. Dai, *ACS Nano* **2011**, *5*, 1505; b) C. Zhu, Q. Yang, F. Lv, L. Liu, S. Wang, *Adv. Mater.* **2013**, *25*, 1203; c) J. V. Garcia, J. Yang, D. Shen, C. Yao, X. Li, R. Wang, G. D. Stucky, D. Zhao, P. C. Ford, F. Zhang, *Small* **2012**, *8*, 3800; d) M. H. Cho, E. J. Lee, M. Son, J. H. Lee, D. Yoo, J. W. Kim, S. W. Park, J. S. Shin, J. Cheon, *Nat. Mater.* **2012**, *11*, 1038; e) J. H. Lee, K. J. Chen, S. H. Noh, M. A. Garcia, H. Wang, W. Y. Lin, H. Jeong, B. J. Kong, D. B. Stout, J. Cheon, H. R. Tseng, *Angew. Chem.* **2013**, *125*, 4480; *Angew. Chem. Int. Ed.* **2013**, *52*, 4384; f) J. Liu, B. Wang, S. B. Hartono, T. Liu, P. Kantharidis, A. P. Middelberg, G. Q. Lu, L. He, S. Z. Qiao, *Biomaterials* **2012**, *33*, 970; g) S. B. Hartono, W. Gu, F. Kleitz, J. Liu, L. He, A. P. J. Middelberg, C. Yu, G. Q. Lu, S. Z. Qiao, *ACS Nano* **2012**, *6*, 2104.

[8] a) X. Yang, X. Liu, Z. Liu, F. Pu, J. Ren, X. Qu, *Adv. Mater.* **2012**, *24*, 2890; b) C. Chen, L. Zhou, J. Geng, J. Ren, X. Qu, *Small* **2013**, *9*, 2793.

[9] a) B. Tian, C. Wang, S. Zhang, L. Feng, Z. Liu, *ACS Nano* **2011**, *5*, 7000; b) L. Gao, J. Fei, J. Zhao, H. Li, Y. Cui, J. Li, *ACS Nano* **2012**, *6*, 8030; c) W. S. Kuo, C. N. Chang, Y. T. Chang, M. H. Yang, Y. H. Chien, S. J. Chen, C. S. Yeh, *Angew. Chem.* **2010**, *122*, 2771; *Angew. Chem. Int. Ed.* **2010**, *49*, 2711; d) J. Wang, G. Zhu, M. You, E. Song, M. I. Shukoor, K. Zhang, M. B. Altman, Y. Chen, Z. Zhu, C. Z. Huang, W. Tan, *ACS Nano* **2012**, *6*, 5070; e) F. Li, S.-J. Park, D. Ling, W. Park, J. Y. Han, K. Na, K. Char, *J. Mater. Chem. B* **2013**, *1*, 1678.

[10] a) F. Muhammad, M. Guo, W. Qi, F. Sun, A. Wang, Y. Guo, G. Zhu, *J. Am. Chem. Soc.* **2011**, *133*, 8778; b) A. Sasidharan, P. Chandran, D. Menon, S. Raman, S. Nair, M. Koyakutty, *Nanoscale* **2011**, *3*, 3657; c) T. Xia, M. Kovochich, M. Liong, L. Mädler, B. Gilbert, H. Shi, J. I. Yeh, J. I. Zink, A. E. Nel, *ACS Nano* **2008**, *2*, 2121.

[11] a) H. Zhang, B. Chen, H. Jiang, C. Wang, H. Wang, X. Wang, *Biomaterials* **2011**, *32*, 1906; b) Y. Li, W. Zhang, J. Niu, Y. Chen, *ACS Nano* **2012**, *6*, 5164.

[12] a) H. Hayashi, I. V. Lightcap, M. Tsujimoto, M. Takano, T. Umeyama, P. V. Kamat, H. Imahori, *J. Am. Chem. Soc.* **2011**, *133*, 7684; b) Q. P. Luo, X. Y. Yu, B. X. Lei, H. Y. Chen, D. B. Kuang, C. Y. Su, *J. Phys. Chem. C* **2012**, *116*, 8111; c) T. Xu, L. Zhang, H. Cheng, Y. Zhu, *Appl. Catal., B* **2011**, *101*, 382.

[13] a) J. T. Robinson, S. M. Tabakman, Y. Liang, H. Wang, H. Sanchez Casalongue, D. Vinh, H. Dai, *J. Am. Chem. Soc.* **2011**, *133*, 6825; b) K. Yang, L. Hu, X. Ma, S. Ye, L. Cheng, X. Shi, C. Li, Y. Li, Z. Liu, *Adv. Mater.* **2012**, *24*, 1868; c) K. Yang, L. Feng, X. Shi, Z. Liu, *Chem. Soc. Rev.* **2013**, *42*, 530.

[14] a) G. Liu, K. Y. Choi, A. Bhirde, M. Swierczewska, J. Yin, S. W. Lee, J. H. Park, J. I. Hong, J. Xie, G. Niu, D. O. Kiesewetter, S. Lee, X. Chen, *Angew. Chem.* **2012**, *124*, 460–464; *Angew. Chem. Int. Ed.* **2012**, *51*, 445; b) M. Swierczewska, K. Y. Choi, E. L. Mertz, X. Huang, F. Zhang, L. Zhu, H. Y. Yoon, J. H. Park, A. Bhirde, S. Lee, X. Chen, *Nano Lett.* **2012**, *12*, 3613; c) T. Pouyani, G. S. Harbison, G. D. Prestwich, *J. Am. Chem. Soc.* **1994**, *116*, 7515.

[15] a) Y. Luo, M. R. Ziebell, G. D. Prestwich, *Biomacromolecules* **2000**, *1*, 208; b) T. Pouyani, G. D. Prestwich, *Bioconjugate Chem.* **1994**, *5*, 339; c) K. Y. Choi, H. Chung, K. H. Min, H. Y. Yoon, K. Kim, J. H. Park, I. C. Kwon, S. Y. Jeong, *Biomaterials* **2010**, *31*, 106; d) K. Y. Choi, H. Y. Yoon, J. H. Kim, S. M. Bae, R. W. Park, Y. M. Kang, I. S. Kim, I. C. Kwon, K. Choi, S. Y. Jeong, K. Kim, J. H. Park, *ACS Nano* **2011**, *5*, 8591; e) Q. He, M. Ma, C. Wei, J. Shi, *Biomaterials* **2012**, *33*, 4392; f) M. Ma, H. R. Chen, Y. Chen, K. Zhang, X. Wang, X. Z. Cui, J. L. Shi, *J. Mater. Chem.* **2012**, *22*, 5615; g) Z. Chen, Z. Li, Y. Lin, M. Yin, J. Ren, X. Qu, *Biomaterials* **2013**, *34*, 1364; h) Z. Chen, Z. Li, Y. Lin, M. Yin, J. Ren, X. Qu, *Chem. Eur. J.* **2013**, *19*, 1778.

[16] R. Stern, M. J. Jedrzejas, *Chem. Rev.* **2006**, *106*, 818.

[17] a) Y. Song, K. Qu, C. Zhao, J. Ren, X. Qu, *Adv. Mater.* **2010**, *22*, 2206; b) W. S. Hummers, R. E. Offeman, *J. Am. Chem. Soc.* **1958**, *80*, 1339; c) X. Huang, K. Qian, J. Yang, J. Zhang, L. Li, C. Yu, D. Zhao, *Adv. Mater.* **2012**, *24*, 4419; d) S. He, B. Song, D. Li, C. Zhu, W. Qi, Y. Wen, L. Wang, S. Song, H. Fang, C. Fan, *Adv. Funct. Mater.* **2010**, *20*, 453.

[18] R. J. Hunter, *Zeta Potential in Colloid Science: Principles and Applications* Academic Press London **1981**.

[19] W. Zhang, C. Wang, Z. Li, Z. Lu, Y. Li, J. J. Yin, Y. T. Zhou, X. Gao, Y. Fang, G. Nie, Y. Zhao, *Adv. Mater.* **2012**, *24*, 5391.

[20] a) K. Maeda, T. Takata, M. Hara, N. Saito, Y. Inoue, H. Kobayashi, K. Domen, *J. Am. Chem. Soc.* **2005**, *127*, 8286; b) B. Li, T. Liu, Y. Wang, Z. Wang, *J. Colloid Interf. Sci.* **2012**, *377*, 114.

[21] a) A. Abdelhay, T. Carmen-Mihaela, M. Christophe, M. Cédric, G. Hélène, M. Ghouti, S. Raphaël, *Nanotechnol.* **2012**, *23*, 335101; b) J. Li, M. Huo, J. Wang, J. Zhou, J. M. Mohammad, Y. Zhang, Q. Zhu, A. Y. Waddad, Q. Zhang, *Biomaterials* **2012**, *33*, 2310.